Quantum Electronics **52** (4) 343–350 (2022)

https://doi.org/10.1070/QEL18015

Analysis of light–current characteristics of high-power semiconductor lasers (1060 nm) in a steady-state 2D model

S.O. Slipchenko, V.S. Golovin, O.S. Soboleva, I.A. Lamkin, N.A. Pikhtin

Abstract. **This paper presents a 2D model of a high-power semiconductor laser, which takes into account carrier transport across the layers of its heterostructure and longitudinal spatial hole burning (LSHB), an effect related to the nonuniform gain distribution along the cavity axis. We show that the use of the 2D model which takes into account carrier transport across the layers of the heterostructure allows an appreciable contribution of LSHB to saturation of light–current characteristics to be demonstrated. The LSHB effect, causing a decrease in the output optical power of semiconductor lasers, is shown to be stronger at high drive currents and low output mirror reflectivities. In the case of high drive currents, the LSHB-induced drop in power is related to the faster growth of internal optical and recombination losses because of the nonuniform current density distribution along the cavity axis, such that the highest current density can be almost twice the lowest one. LSHB is shown to increase the power stored in a Fabry–Perot cavity, which is an additional mechanism reducing the output optical power.**

Keywords: *model of a semiconductor laser, rate equations, carrier transport, longitudinal hole burning, laser diode, high-power semiconductor lasers, drift-diffusion transport.*

1. Introduction

Advanced semiconductor laser power supplies allow one to obtain current pulses hundreds of amperes in amplitude and a few to hundreds of nanoseconds in duration [1–3]. The operation of high-power semiconductor lasers at such drive currents is accompanied by insignificant heating of the active region, which allows for a substantial increase in peak power relative to that in continuous mode [4, 5]. At the same time, light–current (L–I) characteristics of lasers begin to saturate at rather low drive currents [6, 7]. To understand the cause of optical power saturation, experimental and theoretical studies examined a number of mechanisms operative above the lasing threshold: growth of internal optical loss [8], nonlinear gain saturation and growth of threshold concentration [9], two-photon absorption [10], and spatial hole burning along the cavity axis [11, 12]. Direct experimental observation of how these mechanisms operate during lasing is a rather complex technical issue [8, 9, 13]. In view of this, construction of models that describe the operation of semiconductor lasers and take into account these mechanisms will allow one to optimise laser heterostructure parameters and raise the output optical power.

In the last decade, a number of studies have been aimed at constructing such models, including the simplest 1D analytical models relying on the diffusion mechanism of carrier transport in the waveguide layer, which has made it possible to assess the effect of drive current on the internal optical loss above the lasing threshold [14]. Taking into account 1D carrier transport in terms of continuity equations and Poisson's equation helped to more accurately describe carrier accumulation effects [2], and supplementing the transport model with an equation characterising carrier heating in an electric field provided a more detailed insight into the accumulation effects in the presence of a drift current component, which is important in examining the behaviour of semiconductor lasers in strong electric fields, where the drift velocity is saturated [15].

The next step was models that take into account the laser mode field distribution along the cavity axis. The simplest of them neglect specific features of carrier transport and allow one to determine only a part of the contribution related to the nonuniform gain, carrier concentration, and photon density distributions along the cavity. For example, as shown in an analytical model described previously [16, 17], reflectivity asymmetry and the cavity length have a significant effect on the effective lasing threshold and, as a consequence, reduce laser efficiency. (The effective threshold can be evaluated through the carrier distribution in the active region along the cavity length and determines the contribution of the nonuniformity related to spatial hole burning along the cavity.) More complete models that take into account mechanisms of carrier accumulation in layers of a heterostructure, carrier leakage as a result of transport, the laser mode distribution along the cavity, and two-photon absorption were considered in Refs [18–20], where numerical simulation was performed for identical structures, with various commercial software packages used completely or partially. Results obtained for pulsed pumping demonstrate that a considerable contribution to output optical power saturation is made by the loss due to free charge carriers. To reach agreement with experimental data, it was necessary to take into account leakage and longitudinal spatial hole burning (LSHB) [19, 20] or saturation and LSHB [18].

In this work, we model L–I characteristics of high-power semiconductor lasers in pulsed mode using a numerical steady-state 2D model that takes into account carrier trans-

S.O. Slipchenko, V.S. Golovin, O.S. Soboleva, N.A. Pikhtin Ioffe Institute, Russian Academy of Sciences, Politekhnicheskaya ul. 26, 194021 St. Petersburg, Russia;
e-mail: soboleva@mail.ioffe.ru, Serghpl@mail.ioffe.ru, vsgolovin@mail.ioffe.ru, Nike@hpld.ioffe.ru;
I.A. Lamkin Saint Petersburg Electrotechnical University LETI, ul. Prof. Popova 5, 197376 St. Petersburg, Russia

Received 3 December 2021; revision received 21 December 2021
Kvantovaya Elektronika **52** (4) 343–350 (2022)
Translated by O.M. Tsarev

port in the heterostructure and effects related to the nonuniform photon distribution along the cavity axis, namely, the nonuniform carrier concentration, drive current density, optical loss, and carrier leakage distributions along the cavity axis. The $L-I$ characteristics calculated for laser diodes in the 2D model are compared to results obtained in a 1D model in order to demonstrate the key features and applicability conditions of the models under consideration.

2. Description of the model

To calculate light–current and current–voltage ($I-V$) characteristics of laser diodes, we constructed a steady-state model in which the band diagram and photon concentration are successively calculated at a given voltage, which in turn determines currents flowing through the instrument. The first part of the model is a drift-diffusion model of carrier transport in a semiconductor, which comprises continuity equations for electron and hole current densities (j_n and j_p, respectively) and Poisson's equations. Carrier transport is calculated only in the vertical direction x (i.e. in the growth direction of the epitaxial structure), in the steady-state approximation. As a result, we obtain a 1D steady-state model represented by the following equations:

$$-\frac{\mathrm{d}}{\mathrm{d}x}\left(\varepsilon\varepsilon_0\frac{\mathrm{d}\psi}{\mathrm{d}x}\right) = q(N_\mathrm{d}^+ - N_\mathrm{a}^- - n + p), \tag{1}$$

$$\frac{\mathrm{d}j_\mathrm{n}}{\mathrm{d}x} = qR, \tag{2a}$$

$$\frac{\mathrm{d}j_p}{\mathrm{d}x} = -qR, \tag{2b}$$

$$j_\mathrm{n} = -q\mu_\mathrm{n} n\frac{\mathrm{d}\psi}{\mathrm{d}x} + qD_\mathrm{n}\frac{\mathrm{d}n}{\mathrm{d}x}, \tag{3a}$$

$$j_\mathrm{p} = -q\mu_\mathrm{p} p\frac{\mathrm{d}\psi}{\mathrm{d}x} - qD_\mathrm{p}\frac{\mathrm{d}p}{\mathrm{d}x}, \tag{3b}$$

where n and p are free electron and hole concentrations, respectively; ψ is the electrostatic potential; N_d^+ and N_a^- are the concentrations of ionised donor and acceptor impurities, respectively; R is the recombination rate; q is the elementary charge; ε is dielectric permittivity; ε_0 is the electric constant; μ_n and μ_p are electron and hole mobilities, respectively; and D_n and D_p are the electron and hole diffusion coefficients, which were calculated through carrier mobilities using Einstein's relations.

The recombination rate R was found as

$$R = R_\mathrm{SRH} + R_\mathrm{rad} + R_\mathrm{Aug} + R_\mathrm{st}, \tag{4}$$

where R_rad, R_SRH, and R_Aug are the radiative, Shockley–Read–Hall, and Auger recombination rates, respectively, and the stimulated recombination rate R_st is given by

$$R_\mathrm{st} = v_\mathrm{g}\frac{MG\omega}{D}S. \tag{5}$$

Here, G is the material gain [see Eqn (6)]; S is photon concentration [see (8) and (9)]; v_g is the group velocity of photons in the cavity; M is the laser mode profile [see (7)]; and ω is the frequency of light.

To describe lasing, the drift-diffusion system was modified as follows: In the 1D case, lasing is described by a lumped equation, as in an earlier study [17], so the solution can be described by a single quantity – photon concentration in the waveguide, S – and the functions $\psi(x)$, $n(x)$ and $p(x)$. In the 2D case, all the above parameters are functions of the longitudinal coordinate y (along the cavity axis). Neighbouring points along the y axis are then only connected through photon concentration, and longitudinal carrier transport is left out of consideration. Such a simplification is not critical because, with the problem formulation we use, transport along the y axis is in most cases negligible. The shape of the optical mode across the layers of the heterostructure was calculated using the wave equation.

The material gain G was calculated using the relation

$$G(n,p) = G_0\ln\frac{\min(n,p)}{n_\mathrm{tr}}, \tag{6}$$

where the gain coefficient G_0 and transparency concentration n_tr are characteristics of the active region. Gain model parameters were found by fitting experimental material gain data for an InGaAs quantum well with $\lambda = 1060$ nm.

In rate equations, the modal gain g is usually represented as the product of the material gain G, dependent on the free electron and hole concentration in the active region, and the optical confinement factor Γ, which quantifies the overlap of the laser mode with the active region. In calculating vertical transport, this approximation is replaced by the relation

$$g = \frac{1}{D}\int_{\mathcal{X}_\mathrm{a}} MG\,\mathrm{d}x, \tag{7}$$

where M is the laser mode profile; $\mathcal{X}_\mathrm{a}$ is the thickness of the active region of the laser; and D is a characteristic thickness given by

$$\frac{1}{D}\int_{\mathcal{X}_\mathrm{a}} M\,\mathrm{d}x = 1.$$

Thus, this relation takes into account the nonuniform electron and hole distributions in the active region, which can be essential in the case of structures with multiple quantum wells or a bulk active region.

The rate equations in the 2D model include the functions $S_+(y)$ and $S_-(y)$: concentrations of photons moving in the forward and backward directions along the y axis of the cavity. Here S represents the integrated photon concentration (along the x axis) in each of the m segments and is thus measured in inverse square centimetres.

$$\frac{1}{v_\mathrm{g}}\frac{\mathrm{d}S_+}{\mathrm{d}t} = -\frac{1}{v_\mathrm{g}}\frac{\mathrm{d}S_+}{\mathrm{d}y} + (g - \alpha_\mathrm{FCA})S_+ + \frac{\beta_\mathrm{sp}}{2}R_\mathrm{rad} = 0, \tag{8}$$

$$\frac{1}{v_\mathrm{g}}\frac{\mathrm{d}S_-}{\mathrm{d}t} = \frac{1}{v_\mathrm{g}}\frac{\mathrm{d}S_-}{\mathrm{d}y} + (g - \alpha_\mathrm{FCA})S_- + \frac{\beta_\mathrm{sp}}{2}R_\mathrm{rad} = 0, \tag{9}$$

where α_FCA is the free-carrier internal optical loss; L is the cavity length; and β_sp is the spontaneous emission factor, i.e.

the fraction of spontaneous emission in the laser mode. To solve the problem, the cavity is divided into m segments and S_+ and S_- are set at their boundaries. As a result, the system of differential equations describing transport in the 2D model includes equations of the form (1)–(3) for each segment, with a total of $3m$ equations.

The values of $S_{-|y=0}$ and $S_{+|y=L}$ corresponding to the cavity boundaries and found by solving the system of equations can be used to calculate the output optical power for both mirrors of the laser:

$$P_1 = \frac{hc}{\lambda}(1 - R_{AR})v_g DwS_{-|y=0}, \quad (10)$$

$$P_2 = \frac{hc}{\lambda}(1 - R_{HR})v_g DwS_{+|y=L}. \quad (11)$$

Here R_{AR} and R_{HR} are the reflectivities of the mirrors; hc/λ is the photon energy (where h is the Planck constant; c is the speed of light; and λ is the laser wavelength); and w is the width of the stripe contact.

In this study, to analyse operation conditions of semiconductor lasers at high drive currents, we examined an asymmetric heterostructure with a low internal optical loss at the lasing threshold, such as are widely used in the fabrication of semiconductor lasers. The heterostructure consisted of 2-μm-thick $Al_xGa_{1-x}As$-based (x = 30%) heavily doped N and P emitters, a 1.7-μm-thick undoped $Al_xGa_{1-x}As$ (x = 10%) waveguide, and a 9-nm-thick quantum-confined InGaAs active region emitting at 1060 nm and sandwiched between 10-nm-thick GaAs spacers. The active region was located closer to the P emitter, so that the distance to the P_+ layer was 0.65 μm. The parameters characterising carrier transport and generation–recombination processes in the heterostructure and the design of the laser diodes analysed in the 2D model under consideration are given below:

Electron mobility in the emitters, $\mu_{n,em}$/cm^2 V^{-1} s^{-1}	1700
Electron mobility in the waveguide, $\mu_{n,wg}$/cm^2 V^{-1} s^{-1}	2700
Hole mobility in the emitters, $\mu_{p,em}$/cm^2 V^{-1} s^{-1}	120
Hole mobility in the waveguide, $\mu_{p,wg}$/cm^2 V^{-1} s^{-1}	150
Shockley–Read–Hall lifetime of electrons and holes, $\tau_{n,p}$/ns	10
Radiative recombination coefficient, B/cm^3 s^{-1}	2×10^{-10}
Auger recombination coefficient, $C_{n,p}$/cm^6 s^{-1}	2×10^{-30}
Cavity length, L/μm	3000
Stripe contact width, w/μm	100
Reflectivity of the output mirror ($y = 0$), R_{AR}	0.1%–5%
Reflectivity of the back mirror ($y = L$), R_{HR}	99%
Gain coefficient, G_0/cm^{-1}	2200
Transparency concentration, n_{tr}/cm^{-3}	1.5×10^{18}
Absorption cross section for electrons, σ_n/cm^2	4×10^{-18}
Absorption cross section for holes, σ_p/cm^2	12×10^{-18}
Refractive index of the emitter layers, n_{em}	3.3954
Refractive index of the waveguide layer, n_{wg}	3.4454
Refractive index of the spacers, n_{spac}	3.4807
Ratio of the band offset at the heterojunctions to the band gap, dE_c/dE_g	0.6
Number of segments along the cavity axis, m	30

To calculate distributions along the y axis, the cavity was divided into 30 segments (m = 30). Thus, the 2D model under consideration is represented by a set of $3m$ equations coupled by boundary conditions. In each segment, we solve the transport equations (1)–(3), which allow us to find carrier distributions in the layers of the heterostructure at various drive currents, and the rate equations (6) and (7) for photons, which determine the stimulated recombination rate R_{st}, appearing in the total recombination rate R in the transport equations.

As shown above, the proposed 2D model uses the steady-state approximation, which can be thought to be valid if lasers are pumped by pulses of about 100 ns duration, considerably exceeding the characteristic time of transient processes in semiconductor lasers. On the other hand, such a pulse duration is insufficient for thermal heating of a laser diode, so it can be neglected despite the rather high drive current density.

3. Simulation results

Figure 1 shows L–I characteristics calculated in the 2D model for lasers at different reflectivities of their output mirror (R_{AR} = 0.1%, 1%, and 5%). Also shown for comparison are L–I characteristics calculated in the 1D model, which takes into account only carrier transport along the x axis and, as a consequence, the growth of the internal optical loss and parasitic recombination. It is seen from Fig. 1 that taking into account longitudinal hole burning has a significant effect on calculation results. This primarily manifests itself in that, in the 1D model, the increase in output coupling losses as a result of a decrease in R_{AR} leads to an increase in peak power over the entire range of drive currents under consideration. At the same time, calculations in the 2D model show that there is an optimal output mirror reflectivity R_{AR} that allows the maximum peak emission power at a given drive current to be reached and that the case of the minimum reflectivity R_{AR} = 0.1% considered by us is characterised by sharp saturation of the L–I characteristic even in its initial portion and by the minimum output optical power (Fig. 1).

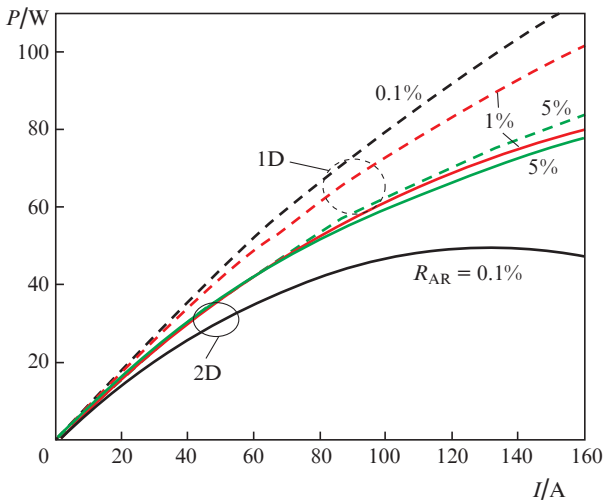

Figure 1. Light–current curves of laser diodes with output mirror reflectivities R_{AR} = 0.1%, 1%, and 5%, calculated using the 2D (solid lines) and 1D (dashed lines) models.

Consider the interrelationship between generation–recombination processes in the 2D model. As described above, in the proposed 2D model the cavity is represented as a sequence of m segments along the y axis, the same voltage is applied to each segment, and transport along the x axis and carrier distributions in the layers of the heterostructure are calculated separately for each segment using the system of transport equations (1)–(3). It is seen in this case that the key processes which determine the carrier concentration in the active region in the ith segment along the y axis of the cavity at a given operating voltage are spontaneous and nonradiative recombination, as well as stimulated recombination, whose rate is related by the rate equations (8) and (9) to the optical gain (a function of carrier concentration in the active region), losses, and stimulated photon concentration. Neighbouring segments are, in turn, linked through photon concentrations on their boundaries, and the difference between the photon concentration at the output of the ith segment and that at its input is determined by the material gain. It is then clear that it is the optical gain and the optical output coupling losses which are responsible for the nonuniform photon distribution in the cavity, which in turn leads to nonuniform recombination rate and, as a consequence, nonuniform carrier concentration distributions in the layers of the heterostructure, and also to nonuniform current density distributions in all m segments along the y axis. In other words, even if the same bias voltage is applied to each segment, there are nonuniform current and concentration distributions along the cavity axis as a result of the optical gain and the nonlinear coupling between it and the carrier concentration in the active region.

Consider in greater detail the mechanisms in question and their effect on the saturation of L–I characteristics. In what follows, we analyse dependences and distributions obtained for the highest drive current, 150 A. First, we determine the optical confinement factor of the laser mode in the ith segment as the ratio of the number of photons in it to the total number of photons in the cavity:

$$\Gamma_i = \frac{S_i}{\sum_{i=0}^{i=m} S_i}, \qquad (12)$$

where S_i is the number of photons in this segment. The Γ_i distributions along the y axis in Fig. 2 illustrate how the reflectivity asymmetry of the cavity mirrors influences the nonuniformity of the photon distribution along the cavity. As would be expected, Γ_i is smallest near the back mirror of the cavity ($y = L = 0.30$ cm), where the reflectivity of the mirror is highest ($R_{HR} = 99\,\%$). Of all the possibilities considered, the smallest optical confinement factor at the back mirror, $\Gamma_i = 0.006$, corresponds to the lowest back mirror reflectivity: $R_{AR} = 0.1\,\%$. Moreover, the ratio of the Γ_i at the output mirror ($y = 0$) to the Γ_i at the back mirror rises from 2.3 to 15 as R_{AR} decreases from 5% to 0.1%.

Another consequence of the decrease in R_{AR} is a considerable growth of carrier concentration in the active region near the back mirror of the cavity (Fig. 3). At the same time, the carrier concentration at the output mirror ($y = 0$) is the lowest and varies insignificantly.

The photon and charge carrier distributions in the active region along the cavity axis have a significant effect on the current density distribution. It is seen in Fig. 4 that, in the

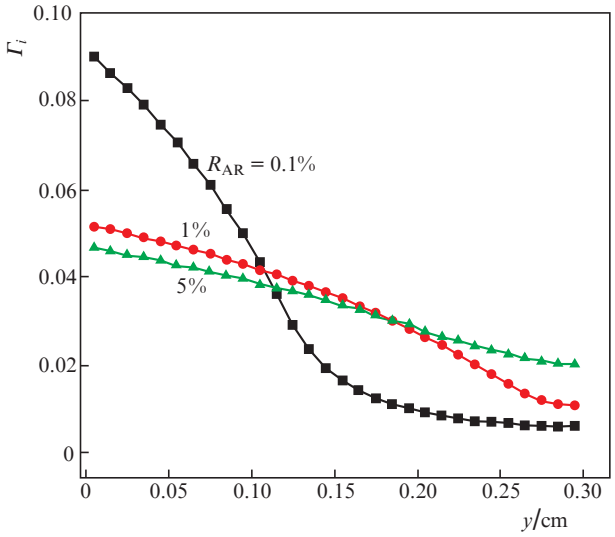

Figure 2. Optical confinement factor (Γ_i) distributions along the cavity axis at output mirror reflectivities $R_{AR} = 0.1\,\%$, 1%, and 5% and a drive current of 150 A.

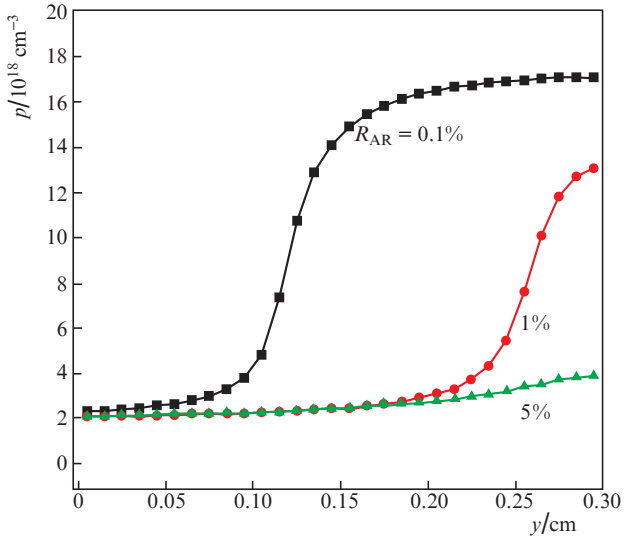

Figure 3. Hole concentration distributions along the cavity axis at output mirror reflectivities $R_{AR} = 0.1\,\%$, 1%, and 5% and a drive current of 150 A.

case of the lowest reflectivity $R_{AR} = 0.1\,\%$, even the highest observed carrier concentration in the active region near the back mirror fails to ensure the highest current density in this region of the cavity. As mentioned above, current density depends on all the recombination processes that occur in the segment under consideration. In the case of the lowest reflectivity $R_{AR} = 0.1\,\%$, photon concentration near the back mirror is lower than that at other (higher) R_{AR} values, which leads to the lowest stimulated recombination rate. The opposite situation occurs at the highest R_{AR} (5%): spontaneous recombination rates are low and the main process is stimulated recombination. As a result, the current density in the region of the cavity under consideration varies little. The highest current density near the back mirror occurs at the intermediate reflectivity $R_{AR} = 1\,\%$, which is due to the suffi-

ciently large contribution of both spontaneous and stimulated recombination. A characteristic feature of the obtained current density distributions along the cavity axis is the rather sharp transition from the high current density region to the low current density region in the case of the low output mirror reflectivities (0.1% and 1%) (Fig. 4), which reproduces key features of the carrier concentration distributions in the active region (Fig. 3). Moreover, in lasers differing in R_{AR}, the current density near the output mirror, where a defining contribution is made by the stimulated recombination rate, is determined by photon concentration [Eqn (8), Figs 1, 4].

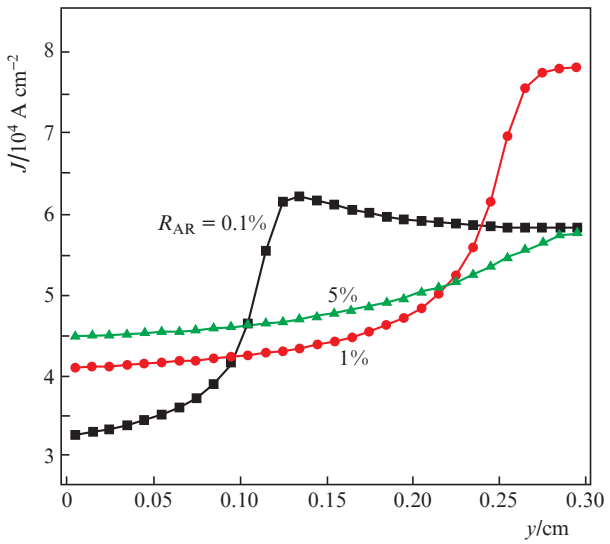

Figure 4. Current density distributions along the cavity axis at output mirror reflectivities R_{AR} = 0.1%, 1%, and 5% and a drive current of 150 A.

The above data make it possible to analyse the material and modal internal optical loss distributions along the cavity axis (Fig. 5). In the model under consideration, the material internal optical loss in the ith segment is completely determined by free-carrier absorption ($\alpha_i = \alpha_{FCA\,i}$). In each segment, $\alpha_{FCA\,i}$ is determined by the overlap integral between the local carrier concentration distributions in the layers of the heterostructure, which depend on the doping level or flowing current, and the field distribution of the laser mode M formed by the transverse waveguide of the heterostructure. It is quite natural that the largest optical loss corresponds to the region near the back mirror (Fig. 5a) because it is this region which has the highest carrier concentration in the active region (Fig. 3) and the highest local current density (Fig. 4) (in the case R_{AR} = 0.1%, the highest current density is shifted to the central region of the cavity, but it is only slightly higher than the current density near the back mirror). It is important to note here that the large optical loss is due to not only the loss in the active region but the loss in the waveguide layers because of the free-carrier accumulation as a result of the flowing current and carrier delocalisation from the active region. Near the output mirror, the material internal optical loss varies rather little with R_{AR} (3.6–4.4 cm^{-1}) and has the lowest value at R_{AR} = 0.1%, suggesting that a defining contribution is made by the waveguiding loss, related to carrier transport (Fig. 5a).

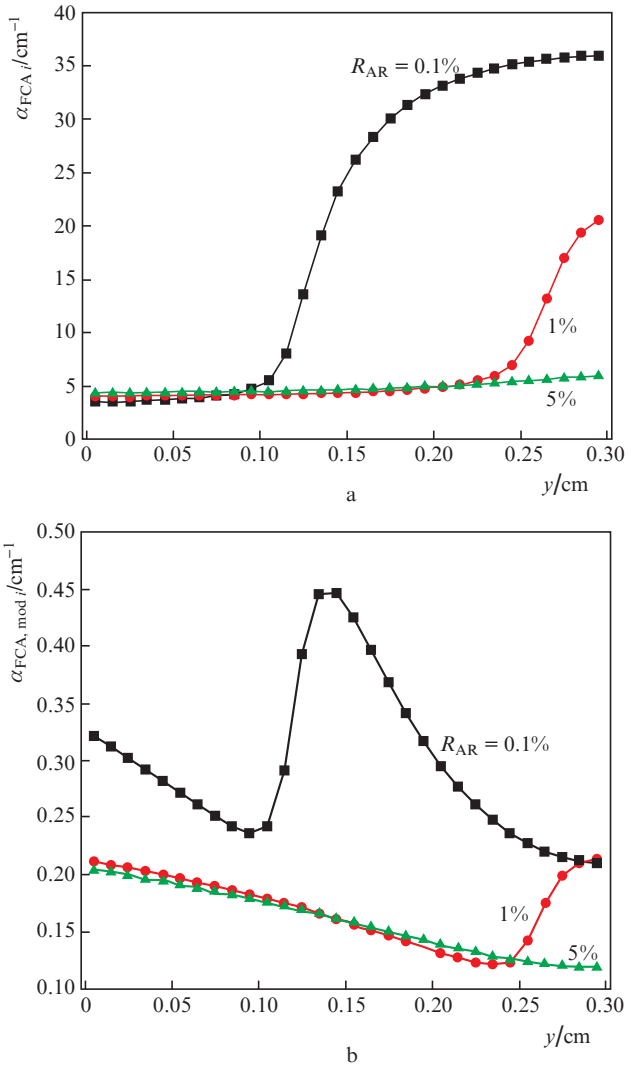

Figure 5. (a) Material and (b) modal internal optical loss distributions along the cavity axis at output mirror reflectivities R_{AR} = 0.1%, 1%, and 5% and a drive current of 150 A.

To evaluate the contribution of the modal loss to the emitted power, we represent the modal internal optical loss $\alpha_{FCA,\,mod}$ as

$$\alpha_{FCA,\,mod} = \sum_{i=0}^{m} \alpha_{FCA,\,mod\,i}\,, \tag{13a}$$

$$\alpha_{FCA,\,mod\,i} = \alpha_{FCA\,i}\Gamma_i\,, \tag{13b}$$

where $\alpha_{FCA,\,mod\,i}$ is the modal optical loss in the ith segment. The calculated $\alpha_{FCA,\,mod\,i}$ distributions along the cavity axis are presented in Fig. 5b. It is seen that the large material optical loss at the back mirror (Fig. 5a) is compensated for by the small number of photons, as evidenced by the small optical confinement factor Γ_i in this part of the cavity (Fig. 2), which eventually determines the low level of modal internal optical losses. It is worth noting that, in the general case, a decrease in output mirror reflectivity can lead to the formation of rather complex $\alpha_{FCA,\,mod\,i}$ distributions along the cavity, with

local minima and maxima in the interior of the cavity (Fig. 5b, R_{AR} = 0.1% and 1%). The calculated modal internal optical loss $\alpha_{FCA,mod}$ is 8.84 cm^{-1} at R_{AR} = 0.1%, 5.06 cm^{-1} at R_{AR} = 1%, and 4.77 cm^{-1} at R_{AR} = 5% (Fig. 5b).

Another important characteristic determining laser efficiency is the internal quantum yield of stimulated recombination. For the structure under study, it can be defined as the ratio of the stimulated recombination current to the total drive current. In our case, carrier leakage to the wide band gap emitters can be neglected, and the decrease in the internal quantum yield at high currents is due to the rise in the rates of spontaneous and nonradiative recombination in the active region and waveguide, which determine the loss current density J_{loss} in the cavity region chosen. J_{loss} distributions along the cavity axis are shown in Fig. 6. As expected, the highest J_{loss} corresponds in all cases to the cavity region near the back mirror, where the carrier concentration is highest in both the active region (Fig. 3) and waveguide. Moreover, the high carrier concentration in the active region and waveguide in the case of the lowest output mirror reflectivity (R_{AR} = 0.1%) leads to a sharp drop in internal quantum yield, down to 54% (Table 1). This can be thought of as a factor determining the decrease in total radiant efficiency at high drive currents and the lowest R_{AR} and treated as an indirect effect of LSHB on the radiant efficiency at high drive currents. The calculated loss current I_{loss} is 68.7 (R_{AR} = 0.1%), 15.5 (1%), and 10.6 A (5%).

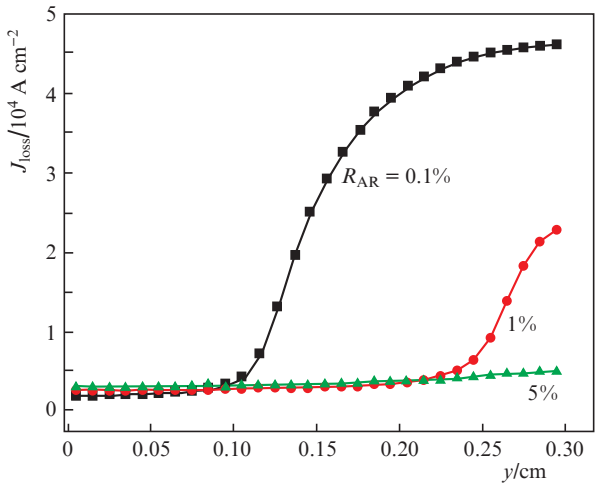

Figure 6. Recombination loss current density distributions along the cavity axis at output mirror reflectivities R_{AR} = 0.1%, 1%, and 5% and a drive current of 150 A.

In conclusion, let us compare the characteristics of semiconductor lasers obtained by calculations in the 1D and 2D models at the highest current (150 A) (Table 1). In the general case, the output optical power can be determined using the relation [21]

$$P(I) = \frac{h\nu}{q}\eta_{in}(I)\eta_d I, \qquad (14)$$

where $h\nu/q$ is the photon energy; $\eta_{in}(I) = (I - I_{loss})/I$ is the internal quantum efficiency; and $\eta_d = \alpha_m/(\alpha_m + \alpha_{in})$ is the slope efficiency (where $\alpha_m = (1/2L)\ln[1/(R_{AR}R_{HR})]$) is the output coupling loss). Calculation in the 1D model suggests that the rise in internal optical loss at high drive currents can be compensated for and the output peak power can be raised by increasing the output coupling loss α_m due to low output mirror reflectivity (in our case, R_{AR} = 0.1%). This calculation result in the 1D model is due to the use of the approximation in which the material gain and current density do not vary along the cavity axis. Comparison with the calculation results in the 2D model shows that this simplification is only justified at sufficiently high output mirror reflectivities (in our case, at R_{AR} > 5% and a cavity length L = 3 mm), when nonuniformities of the photon and carrier concentration distributions along the cavity axis are insignificant and the differential gain is high. In the opposite case, the use of the 1D model leads to a considerable overestimation of the output optical power as the output mirror reflectivity decreases (i.e. at R_{AR} < 5% and L = 3 mm).

Table 1. Simulation and calculation results for laser parameters in the 1D and 2D models.

Parameter	Model	R_{AR} = 0.1%	R_{AR} = 1%	R_{AR} = 5%
I_{loss}/A	1D	12.7	11.7	11.3
	2D	68.7	15.5	10.6
α_{FCA}/cm^{-1}	1D	5.35	5.08	4.9
	2D ($\alpha_{FCA,mod}$)	8.84	5.06	4.77
α_m/cm^{-1}	1D	11.53	7.68	5.0
	2D ($\alpha_{m\,eff}$)	9.69	5.25	4.37
η_d	1D	0.68	0.6	0.51
	2D* (14)	0.52	0.50	0.48
η_{in}	1D	0.91	0.92	0.92
	2D* (14)	0.54	0.9	0.93
P/W	1D	109	97	80.9
	2D**	48.8	77.9	74.7
	2D* (14)	49.7	80.1	78

Note: *, calculation; **, numerical simulation.

To provide the most detailed insight into all loss mechanisms, the output optical power can be estimated using relation (14) and parameters calculated in the 2D model (Table 1). However, here we cannot use the classic relation for calculating the output coupling loss α_m, which was derived for constant gain and current density along the cavity. Because of this, we consider an effective output coupling loss $\alpha_{m\,eff}$ as the ratio of the concentration of photons leaving the cavity through the front mirror, $S_{-|y=0}(1 - R_{AR})$, to the total integrated photon concentration in the cavity:

$$\alpha_{m\,eff} = \frac{S_{-|y=0}(1 - R_{AR})}{\sum_{i=0}^{i=m} S_i}. \qquad (15)$$

The $\alpha_{m\,eff}$ values thus obtained are lower than the α_m calculated in the 1D model. The influence of longitudinal hole burning can be clearly illustrated by comparing the photon distributions along the cavity axis in the 1D and 2D models (Fig. 7a). Thus, this effect contributes to not only various direct losses but also photon accumulation in the cavity. This can be regarded as an additional mechanism of indirect losses, which can be expressed through the effective output coupling loss $\alpha_{m\,eff}$. The power P obtained in the 2D model (Fig. 1) and the values calculated using (14) and the effective output coupling loss (15) are in reasonable agreement (Fig. 7b).

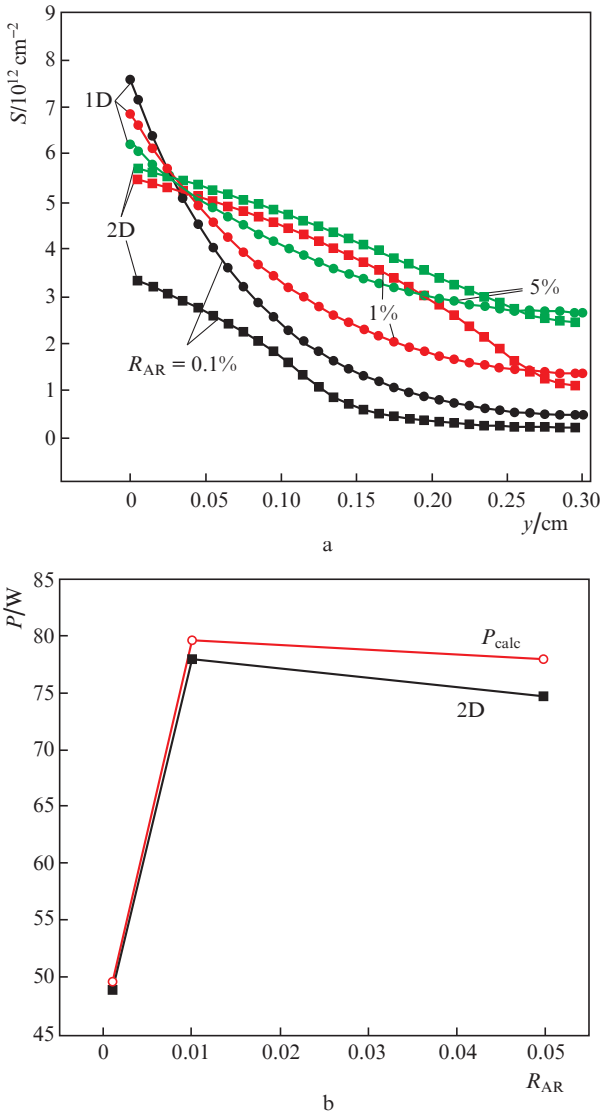

Figure 7. (a) Photon concentration distributions in the cavity obtained in the 1D and 2D models and (b) output optical power distributions calculated in the 2D model (black squares and lines) and using relation (14) and the values of $\alpha_{m\,eff}$, $\alpha_{FCA,\,mod}$ and η_{in} obtained in the 2D model (red circles and lines) at different reflectivities R_{AR}.

4. Conclusions

The present calculation results demonstrate that LSHB is the main cause of the reduced output optical power in high-power semiconductor lasers with severe cavity mirror reflectivity asymmetry and high output mirror transmission, which can show up as both an increase in recombination loss and leakage currents and a more pronounced growth of internal optical loss. This means that, to maximise the peak power at a given drive current, one should optimise laser diode parameters (cavity length, reflectivity of the mirrors, optical confinement factor in the active region, and others) in a model that takes into account LSHB. The contribution of LSHB to optical power saturation can only be adequately assessed in a 2D model that takes into account carrier transport and carrier accumulation in the layers of the heterostructure, as illustrated in Fig. 1 and analysed in Section 3. Taking into account carrier transport across the layers of the heterostructure demonstrates that LSHB makes an appreciable contribution to saturation of light–current characteristics.

The application area of the proposed model is not limited to the heterostructure considered in this study. In particular, the described 2D model can be used in calculations for lasers based on other materials (e.g. on InGaAsP/In) and for structures with an active region based on a bulk layer or a few quantum wells. Further development of the proposed model may include the use of a model for the spectral dependence of gain based on quantum-mechanical calculations of energy levels in a well (kp approximation), with examples in Refs [22–24]. The use of such a model of gain will enable calculations with no reference to experimental data for already existing structures.

Acknowledgements. The construction of the 2D model and analysis of semiconductor lasers with the use of the model were supported by the Russian Science Foundation (Grant No. 19-79-30072). The study of semiconductor lasers with the use of the 1D model was supported by the RF Ministry of Science and Higher Education (State Research Task No. 075-01024-21-00, Project No. FSEE-2020-0008).

References

1. Vainshtein S., Zemlyakov V., Egorkin V., Maslevtsov A., Filimonov A. *IEEE Trans. Power Electron.*, **34**, 3689 (2018).
2. Wang X., Crump P., Wenzel H., Liero A., Hoffmann T., Pietrzak A., Schultz Ch.M., Klehr A., Ginolas A., Einfeldt S., Bugge F., Erbert G., Tränkle G. *IEEE J. Quantum Electron.*, **46**, 658 (2010).
3. Vinokurov D.A., Kapitonov V.A., Lyutetsky A.V., Pikhtin N.A., Slipchenko S.O., Sokolova Z.N., Stankevich A.L., et al. *Semiconductors*, **41**, 984 (2007) [*Fiz. Tekh. Poluprovodn.*, **41**, 1003 (2007)].
4. Pietrzak A., Crump P., Wenzel H., Staske R., Erbert G., Tränkle G. *Semicond. Sci. Technol.*, **24**, 035020 (2009).
5. Veselov D.A., Shashkin I.S., Bobretsova Yu.K., Bakhvalov K.V., Lyutetskiy A.V., Kapitonov V.A., Pikhtin N.A., Slipchenko S.O., Sokolova Z.N., Tarasov I.S. *Semiconductors*, **50**, 1396 (2016) [*Fiz. Tekh. Poluprovodn.*, **50**, 1414 (2016)].
6. Veselov D.A., Kapitonov V.A., Pikhtin N.A., Lyutetskiy A.V., Nikolaev D.N., Slipchenko S.O., Sokolova Z.N., Shamakhov V.V., Shashkin I.S., Tarasov I.S. *Quantum Electron.*, **44**, 993 (2014) [*Kvantovaya Elektron.*, **44**, 993 (2014)].
7. Wang X., Crump P., Pietrzak A., Schultz C., Klehr A., Hoffmann T., Liero A., Ginolas A., Einfeldt S., Bugge F., Tränkle G. *Proc. SPIE*, **7198**, 71981G (2009).
8. Veselov D.A., Bobretsova Y.K., Leshko A.Y., Shamakhov V.V., Slipchenko S.O., Pikhtin N.A. *J. Appl. Phys.*, **126**, 213107 (2019).
9. Bennett A.J., Clayton R.D., Xu J.M. *J. Appl. Phys.*, **83**, 3784 (1998).
10. Avrutin E.A., Ryvkin B.S. *Semicond. Sci. Technol.*, **32**, 015004 (2016).
11. Demir A., Peters M., Duesterberg R., Rossin V., Zucker E. *IEEE Photonics Technol. Lett.*, **27**, 2178 (2015).
12. Wenzel H. *IEEE J. Sel. Top. Quantum Electron.*, **19**, 1 (2013).
13. Veselov D.A., Bobretsova Y.K., Klimov A.A., Bakhvalov K.V., Slipchenko S.O., Pikhtin N.A. *Semicond. Sci. Technol.*, **36**, 115005 (2021).
14. Ryvkin B., Avrutin E. *Electron. Lett.*, **42**, 1283 (2006).
15. Soboleva O.S., Zolotarev V.V., Golovin V.S., Slipchenko S.O., Pikhtin N.A. *IEEE Trans. Electron Devices.*, **67**, 4977 (2020).
16. Ryvkin B.S., Avrutin E.A. *J. Appl. Phys.*, **109**, 043101 (2011).
17. Golovin V.S., Shashkin I.S., Slipchenko S.O., Pikhtin N.A., Kop'ev P.S. *Quantum Electron.*, **50**, 147 (2020) [*Kvantovaya Elektron.*, **50**, 147 (2020)].
18. Wenzel H., Crump P., Pietrzak A., Wang X., Erbert G., Tränkle G. *New J. Phys.*, **12**, 085007 (2010).
19. Piprek J., Li Z.M. *IEEE Photonics Technol. Lett.*, **30**, 963 (2018).

20. Piprek J. *Opt. Quantum Electron*., **51**, 60 (2019).
21. Coldren L.A., Corzine S.W., Mashanovitch M.L. *Diode Lasers and Photonic Integrated Circuits* (Hoboken, NJ: John Wiley & Sons, 2012) Vol. 218.
22. Asryan L.V., Gun'ko N.A., Polkovnikov A.S., Zegrya G.G., Suris R.A., Lau P.K., Makino T. *Semicond. Sci. Technol*., **15**, 1131 (2000).
23. Piprek J. *Semiconductor Optoelectronic Devices: Introduction to Physics and Simulation* (Amsterdam: Elsevier, 2013).
24. Liu G., Chuang S.L., Park S.H. *J. Appl. Phys*., **88**, 5554 (2000).